

## Numerical study of the Yosida method applied to viscous incompressible internal flows with open boundary conditions

J. SZUMBARSKI

*Institute of Aeronautics and Applied Mechanics  
Warsaw University of Technology  
24 Nowowiejska St.  
00-655 Warszawa, Poland  
e-mail: jasz@meil.pw.edu.pl*

THE YOSIDA METHODS FOR INCOMPRESSIBLE VISCOUS FLOWS are investigated numerically in the aspect of local and global errors of volume conservation. Unsteady Stokes and Navier–Stokes flows past an obstacle inserted into 2D channel are used as the test cases. Open boundary conditions are imposed at the channel's inlet and outlet. The results obtained by the Yosida-based Spectral Element Method (SEM) solvers are compared to the results obtained by the SEM solver using exact factorization of the Uzawa system. Analysis of parametric variation of the velocity divergence and the flow rate errors is presented. It is concluded that switching to higher-order Uzawa methods reduces substantially volume conservation errors and removes numerical artifacts observed at the channel's inlet when the basic Yosida method is used.

**Key words:** Navier–Stokes equations, Yosida method, spectral element method, open boundary conditions.

Copyright © 2016 by IPPT PAN

### 1. Introduction

NUMERICAL SOLUTION OF THE NAVIER–STOKES SYSTEM for an incompressible fluid requires specialized algorithms due to zero-divergence constrain imposed on the velocity field. Different approaches have been proposed during last few decades, but they have one common feature – they are typically based on a splitting concept. It means that the update of velocity and pressure fields in one time step is performed in separate sub-steps. The splitting procedure can be applied directly to the original fully-coupled PDE model (differential splitting), which leads to the sequence of a one-way coupled auxiliary differential problems to be solved in each time step. Alternatively, the splitting technique – typically an exact or approximate block-LU factorization – can be applied to an algebraic system obtained from spatial discretization of the original fully-coupled PDE model.

The differential splitting methods can be divided into two categories: the projection schemes and pressure approximation schemes. In the projection schemes,

two velocity-like vector fields appear: the pseudo-velocity which satisfies exactly the boundary conditions but violates the incompressibility constrain (i.e., its divergence is not equal zero) and the “real” velocity, which is divergence-free but fails to satisfy exactly the no-slip condition at the solid walls. The real velocity is obtained via Hodge decomposition applied to the pseudo-velocity, i.e. by the orthogonal projection of the latter on the space of divergence-free vector field. Actually, the Poisson equation must be solved at this stage of simulation. Depending on the particular variant of a projection method, the solution of this equation serves as either the updated pressure or its increment in a time step or it is just an auxiliary scalar field used later to determine the pressure. Detailed exposition of different variants of the projection methods and their mathematical properties can be found in the overview paper by GUERMOND, MINEV and SHEN [1] and also in the presentation [2].

An alternative approach is to build a numerical method based on the usage of the Pressure Poisson Equation. In such method, the explicit divergence constrain (the continuity equation) is replaced by the elliptic problem for the pressure field with appropriately chosen Neumann boundary conditions. It can be shown that the velocity field obtained as the solution to such re-formulated flow problem is indeed divergence-free if only it is such at the initial time instant. In numerical realization, the Navier–Stokes and Pressure Poisson Equations are typically cast into weak forms and solved one after another at each time step. This procedure requires extrapolation of either pressure or velocity dependently of the order in which these equations are solved. This method, known also as the Pressure Approximation Scheme (PAS) and described in details in JOHNSTON and GUO-LIU in [3], is not a projection method because the approximate velocity is not exactly divergence-free. Nevertheless, the divergence error is under control of the time step, and the numerical evidence shows that PAS method can provide second-order time accuracy for both velocity and pressure. Further analysis of the stability and convergence properties of the PAS method can be found in [4], where the stable computations with the third-order method were demonstrated.

In an algebraic splitting approach, one transforms the time/space discretized Stokes or Navier–Stokes system (in the original form, i.e., with the continuity equation explicitly included) to a sequence of more tractable algebraic problems. It is achieved by resorting to some variant of exact or inexact block factorization of the (otherwise coupled) Uzawa system. This approach, going back to the seminal work by PEROT [5], was much developed during last two decades by the EPFL/MOX group (see [6]–[8]) to achieve recently the form of the adaptive high-order Yosida method implemented by VILLA [9] in the ALADINS software. Proponents of this approach usually emphasize its advantages over the differential splitting methods, in particular avoidance of the need for additional and – to

some extent – arbitrary boundary conditions for the differential boundary value problems solved sequentially in each time step. However, it has been shown in [1] that inexact factorization methods enforce implicitly artificial boundary conditions for the pressure (not mentioning that they introduce quasi-compressibility effects) and they are usually no more accurate than the differential splitting methods.

The main goal of this research is to investigate volume conservation properties of the Yosida methods combined with the spectral element discretization and open boundary conditions. An unsteady two-dimensional wall-confined viscous flow past an obstacle is used as a test case. The analysis includes determination of the spatial distribution of the velocity divergence error as well as the global flow rate error, i.e. the difference between the flow rates at the inlet and outlet of the computational domain. Numerical tests have been performed in order to find out how the order of spectral elements, size of the time step and the order of the Yosida method affect local and global volume conservation errors. The in-house spectral element codes have been used in all test simulations. The reference results have been obtained with the code – here referred to as ESEM (Exact Spectral Element Method) – which implements exact solution to the algebraic Stokes system at each time step or, equivalently, uses exact block-LU factorization to solve the Uzawa system. The other code – referred to as YSEM (Yosida Spectral Element Method) – implements the Yosida method of arbitrary order, i.e., the Uzawa system is solved by an appropriately designed inexact block-LU factorization. What concerns the general time marching scheme, both codes use the second-order backward differentiation formula (BDF).

The content of this paper is as follows. In Section 2, we formulate the initial/boundary value problems for Stokes and Navier–Stokes test flows. Both classical and weak forms of these problems are provided. In Section 3, the numerical methods implemented in ESEM/YSEM solvers are described briefly. In Section 4, the main results are presented and discussed. The summary of the research and outlook are included in Section 5. For the sake of self-sufficiency of the presentation, full derivations of the Yosida and Operator-Integration-Factor-Splitting (OIFS) methods have been delivered in the Appendices A and B, respectively.

## 2. Formulation of the test flow problem

The test problem is a nonstationary (pulsatile) flow of an incompressible Newtonian fluid past an obstacle confined between parallel solid walls of a 2D channel, see Figure 1. The boundary  $\partial\Omega$  consists of three parts: the solid wall  $\Gamma_w$  (the channel walls and the contour of the obstacle), the inlet  $\Gamma_{in}$  and the outlet  $\Gamma_{out}$ . The mathematical models of the flow are Stokes ( $\gamma = 0$ ) or the

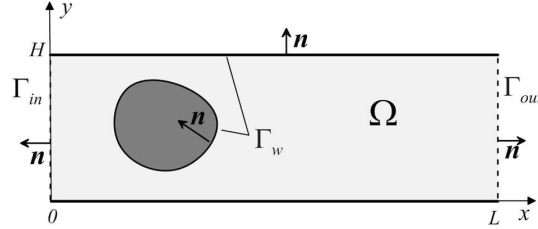


FIG. 1. The flow domain.

Navier–Stokes ( $\gamma = 1$ ) systems

$$(2.1) \quad \begin{cases} \partial_t \mathbf{v} + \gamma(\mathbf{v} \cdot \nabla) \mathbf{v} = -\nabla p + \nu \Delta \mathbf{v}, \\ \nabla \cdot \mathbf{v} = 0. \end{cases}$$

The boundary conditions – the same for both variants – are defined as follows:

$$(2.2) \quad \begin{cases} \mathbf{v} = \mathbf{0} & \text{at } \Gamma_w, \\ p\mathbf{n} - \nu \nabla \mathbf{v} \cdot \mathbf{n} = P_{in}(t)\mathbf{n} & \text{at } \Gamma_{in}, \\ p\mathbf{n} - \nu \nabla \mathbf{v} \cdot \mathbf{n} = \mathbf{0} & \text{at } \Gamma_{out}. \end{cases}$$

Thus, the open boundary conditions are imposed on the inlet section  $\Gamma_{in}$  and the outlet section  $\Gamma_{out}$ . The function  $P_{in}(t)$  is given and describes the time variation of the inlet surface-averaged pressure, i.e.,

$$(2.3) \quad P_{in}(t) = \frac{1}{H} \int_0^H p(t, 0, y) dy,$$

where  $H$  denotes the height of the channel. Also, it can be shown that the open conditions (2.2) imply that

$$\partial_x v_y|_{\Gamma_{in}} = \partial_x v_y|_{\Gamma_{out}} = 0.$$

The initial condition for the flow is  $\mathbf{v}|_{t=0} = \mathbf{v}_0$ , where the initial velocity field should satisfy the continuity condition  $\nabla \cdot \mathbf{v}_0 = 0$ . In all tests in this study, the flow is accelerated from rest, i.e.,  $\mathbf{v}_0 \equiv \mathbf{0}$ , hence this condition is satisfied.

Before the spectral element discretization is applied the boundary value problem (2.1)–(2.2) must be transformed to the weak (variational) form. To this aim, one follows the standard procedure, i.e., the Stokes or the Navier–Stokes equation is multiplied by a test function and integrated over the whole domain  $\Omega$ . After integration by parts of the pressure and viscous terms, the boundary terms appear and the open boundary conditions in (2.2) are plugged

in. Also, the continuity constrain is imposed in a weak sense, i.e., it is demanded that the divergence of the velocity is  $L^2$ -orthogonal to the pressure space. Thus, the weak formulation of the test flow problem can be stated as follows:

Find the velocity field

$$\mathbf{v} \in \mathcal{V} := \{\mathbf{w} \in [H^1(\Omega)]^2, \mathbf{w}|_{\Gamma_w} = \mathbf{0}\}$$

and the pressure field  $p \in L^2(\Omega)$  such that for each vector field  $\mathbf{u} \in \mathcal{V}$  and for each scalar field  $q \in L^2(\Omega)$  the following equalities hold

$$(2.4) \quad \begin{cases} \partial_t \langle \mathbf{v}, \mathbf{u} \rangle + \langle \gamma(\mathbf{v} \cdot \nabla) \mathbf{v}, \mathbf{u} \rangle + \nu \langle \nabla \mathbf{v}, \nabla \mathbf{u} \rangle + P(t) \Phi(\mathbf{u}) - \langle p, \nabla \cdot \mathbf{u} \rangle = 0, \\ \langle \nabla \cdot \mathbf{v}, q \rangle = 0. \end{cases}$$

In the above formulae as well as in the remaining part of the paper, the symbol  $\langle \cdot, \cdot \rangle$  denotes the inner product in the space (either scalar or vector)  $L^2(\Omega)$ . The symbol  $\Phi$  denotes the inlet flux functional, i.e., for each vector field  $\mathbf{u} \in \mathcal{V}$

$$(2.5) \quad \Phi(\mathbf{u}) = \int_{\Gamma_{in}} \mathbf{u} \cdot \mathbf{n} \, dS = - \int_0^1 u_x(t, 0, y) \, dy,$$

where  $u_x$  denotes the  $x$ -component of the vector field  $\mathbf{u}$ .

### 3. Numerical method

The time integration scheme applied to the variational problem (2.4) is the semi-implicit combination of the second-order Backward Differentiation Formula (BDF2) and the two-step Operator-Integration-Factor-Splitting method (OIFS), see [10], [11] and Appendix B. The semi-discrete form of the boundary value problem solved in each time step is

$$(3.1a) \quad \begin{aligned} \frac{3}{2\Delta t} \langle \mathbf{v}^{n+1}, \mathbf{u} \rangle + \nu \langle \nabla \mathbf{v}^{n+1}, \nabla \mathbf{u} \rangle - \langle p^{n+1}, \nabla \cdot \mathbf{u} \rangle, \\ = -P_{in}(t_{n+1}) \Phi(\mathbf{u}) + \frac{1}{\Delta t} [2 \langle \hat{\mathbf{v}}_1^{n+1}, \mathbf{u} \rangle - \frac{1}{2} \langle \hat{\mathbf{v}}_2^{n+1}, \mathbf{u} \rangle], \end{aligned}$$

$$(3.1b) \quad \langle \nabla \cdot \mathbf{v}^{n+1}, q \rangle = 0.$$

In the case of the Stokes flow, we have  $\hat{\mathbf{v}}_1^{n+1} = \mathbf{v}^n$  and  $\hat{\mathbf{v}}_2^{n+1} = \mathbf{v}^{n-1}$ . In the case of the Navier–Stokes flow, the OIFS technique is used, i.e., the symbol  $\hat{\mathbf{v}}_1^{n+1}$  denotes the solution to the following initial value problem (IVP)

$$(3.2) \quad \begin{cases} \frac{d}{dt} \hat{\mathbf{v}}_1 = -(\hat{\mathbf{v}}_1 \cdot \nabla) \hat{\mathbf{v}}_1, & t \in [t_n, t_{n+1}], \\ \hat{\mathbf{v}}_1|_{t=t_n} = \mathbf{v}^n \end{cases}$$

computed at the time instant  $t = t_{n+1}$ . Similarly, the symbol  $\hat{\mathbf{v}}_2^{n+1}$  denotes the value of the solution to the following IVP

$$(3.3) \quad \begin{cases} \frac{d}{dt} \hat{\mathbf{v}}_2 = -(\hat{\mathbf{v}}_2 \cdot \nabla) \hat{\mathbf{v}}_2, & t \in [t_{n-1}, t_{n+1}], \\ \hat{\mathbf{v}}_2|_{t=t_{n-1}} = \mathbf{v}^{n-1} \end{cases}$$

at the same time instant.

The initial value problems (3.2) and (3.3) are integrated numerically by means of the standard fourth-order Runge–Kutta method with the time step  $\Delta t_{\text{RK4}} = \Delta t / M_{\text{RK4}}$ . In this study, the number  $M_{\text{RK4}}$  has been set to 5, which seems to be a good compromise between computational efficiency and numerical stability of the scheme.

The spatial discretization implemented in the in-house solvers used in this study is the Galerkin spectral element method working on quadrilateral grids. The standard Gauss–Legendre (GL) and the Gauss–Legendre–Lobatto (GLL) basic functions are used for the pressure and velocity fields, respectively (see [11], [12]). The local approximation of pressure and velocity fields fulfills the inf-sup condition, meaning that the number of local collocation points for the velocity  $N_V$  and for the pressure  $N_P$  satisfy the relation  $N_P = N_V - 2$ . There are no pressure collocation points at the boundaries of the spectral elements, i.e., the approximate pressure is discontinuous through these boundaries.

The approximate velocity field at the time instant  $t = t_{n+1}$  can be written as

$$(3.4) \quad \mathbf{v}^{n+1} = \left[ \sum_{i=1}^{I_V} (\mathbf{v}_1^{n+1})_i \xi_i \right] \mathbf{e}_1 + \left[ \sum_{i=1}^{I_V} (\mathbf{v}_2^{n+1})_i \xi_i \right] \mathbf{e}_2,$$

where  $\{\xi_i, i = 1, \dots, I_V\}$  are the global GLL basic functions and the  $\mathbf{e}_1$  and  $\mathbf{e}_2$  are the Cartesian unit vectors. The vector coefficients  $\{\mathbf{v}_i^{n+1}, i = 1, \dots, I_V\}$  are the values of the velocity field at the velocity collocation nodes. Analogously, the instantaneous distribution of pressure can be written as

$$(3.5) \quad p^{n+1} = \sum_{i=1}^{I_P} p_i^{n+1} \eta_i,$$

where  $\{\eta_i, i = 1, \dots, I_P\}$  are the global GL basic functions and the scalar coefficients  $\{p_i^{n+1}, i = 1, \dots, I_P\}$  are the values of the pressure field at the pressure collocation nodes.

In order to derive the algebraic linear system solved in each time step, we introduce the following indexed structures

$$(3.6a) \quad (\mathbf{M}_V)_{ij} = \langle \xi_i, \xi_j \rangle \equiv \int_{\Omega} \xi_i \xi_j \, d\mathbf{x}, \quad i, j = 1, \dots, I_V,$$

$$(3.6b) \quad (\mathbf{K}_V)_{ij} = \langle \nabla \xi_i, \nabla \xi_j \rangle \equiv \int_{\Omega} \nabla \xi_i \cdot \nabla \xi_j \, d\mathbf{x}, \quad i, j = 1, \dots, I_V,$$

$$(3.6c) \quad \mathbf{A} = \frac{3}{2\Delta t} \mathbf{M}_V + \nu \mathbf{K}_V,$$

$$(3.6d) \quad (\mathbf{B}_\alpha)_{ij} = -\langle \eta_i, \partial_{x_\alpha} \xi_j \rangle \equiv - \int_{\Omega} \eta_i \frac{\partial \xi_j}{\partial x_\alpha} \, d\mathbf{x},$$

$$i = 1, \dots, I_P, \quad j = 1, \dots, I_V, \quad \alpha = 1, 2,$$

$$(3.6e) \quad (\boldsymbol{\lambda}_\alpha)_i = \Phi(\xi_i \mathbf{e}_\alpha), \quad i = 1, \dots, I_V, \quad \alpha = 1, 2,$$

$$(3.6f) \quad (\mathbf{r}_\alpha^{n+1})_i = \left\langle \frac{2}{\Delta t} \hat{\mathbf{v}}_1^{n+1} - \frac{1}{2\Delta t} \hat{\mathbf{v}}_2^{n+1}, \xi_i \mathbf{e}_\alpha \right\rangle, \quad i = 1, \dots, I_V, \quad \alpha = 1, 2.$$

Then, the algebraic system solved at each time step of the numerical simulation assumes the following form

$$(3.7) \quad \begin{bmatrix} \mathbf{A} & \mathbf{0} & \mathbf{B}_1^\top \\ \mathbf{0} & \mathbf{A} & \mathbf{B}_2^\top \\ \mathbf{B}_1 & \mathbf{B}_2 & \mathbf{0} \end{bmatrix} \begin{bmatrix} \mathbf{v}_1^{n+1} \\ \mathbf{v}_2^{n+1} \\ \mathbf{p}^{n+1} \end{bmatrix} = \begin{bmatrix} \mathbf{r}_1^{n+1} - P_{in}(t_{n+1}) \boldsymbol{\lambda}_1 \\ \mathbf{r}_2^{n+1} - P_{in}(t_{n+1}) \boldsymbol{\lambda}_2 \\ \mathbf{0} \end{bmatrix}$$

A compact form of the system (3.7), which is more convenient for further considerations, reads

$$(3.8) \quad \begin{bmatrix} \mathbf{C} & \mathbf{B}^\top \\ \mathbf{B} & \mathbf{0} \end{bmatrix} \begin{bmatrix} \mathbf{v}^{n+1} \\ \mathbf{p}^{n+1} \end{bmatrix} = \begin{bmatrix} \mathbf{f}^{n+1} \\ \mathbf{0} \end{bmatrix}$$

Clearly,

$$(3.9) \quad \mathbf{C} = \begin{bmatrix} \mathbf{A} & \mathbf{0} \\ \mathbf{0} & \mathbf{A} \end{bmatrix}, \quad \mathbf{B} = [\mathbf{B}_1 | \mathbf{B}_2],$$

$$\mathbf{f}^{n+1} = \begin{bmatrix} \mathbf{r}_1^{n+1} - P_{in}(t_{n+1}) \boldsymbol{\lambda}_1 \\ \mathbf{r}_2^{n+1} - P_{in}(t_{n+1}) \boldsymbol{\lambda}_2 \end{bmatrix}, \quad \mathbf{v}^{n+1} = \begin{bmatrix} \mathbf{v}_1^{n+1} \\ \mathbf{v}_2^{n+1} \end{bmatrix}$$

The standard solution method of system (3.8) contains the following three steps:

**Step 1:** calculation of the pseudo-velocity field

$$(3.10a) \quad \mathbf{C} \tilde{\mathbf{v}} = \mathbf{f}.$$

**Step 2:** calculation of the pressure field

$$(3.10b) \quad \boldsymbol{\Sigma} \mathbf{p} = -\mathbf{B} \tilde{\mathbf{v}}.$$

**Step 3:** calculation of the velocity field

$$(3.10c) \quad \mathbf{C} \mathbf{v} = \mathbf{f} - \mathbf{B}^T \mathbf{p}.$$

The matrix of the linear system (3.10b)

$$(3.11) \quad \boldsymbol{\Sigma} = -\mathbf{B} \mathbf{C}^{-1} \mathbf{B}^T$$

is called the Uzawa (or pressure) matrix.

In this study, the matrices  $\mathbf{C}$  and  $\boldsymbol{\Sigma}$  are symmetric and positive definite, therefore the Conjugate Gradient Method (CGM) is used to all linear systems (3.10). For sufficiently small time step, the matrix  $\mathbf{C}$  is strongly diagonally dominant, thus simple diagonal preconditioning leads to rapid convergence. The solution of the pressure system (3.10b) is much more difficult. First, anytime the matrix-vector product is needed, the linear system with the matrix  $\mathbf{C}$  must be solved in the internal iterative process. Most importantly, the Uzawa matrix is usually very poorly conditioned, hence reaching fast convergence of CGM iterations is not trivial. To this aim, two important elements are incorporated into the in-house solvers used in this study: the two-level pressure preconditioning technique proposed by COUZY *et al.* [13] (from the repertoire of pressure preconditioners considered in that paper, the one actually implemented here is P5) and smart prediction of initial pressure approximation based on the idea proposed originally by FISHER [15].

It should be noted that a different, more stable than OIFS treatment of the convective term will typically lead to a non-symmetric matrix  $\mathbf{C}$ . For instance, the semi implicit approach to the convective term would bring the following form of this matrix

$$(3.12) \quad \mathbf{C} = \frac{3}{2\Delta t} \mathbf{M}_V + \nu \mathbf{K}_V + \mathbf{N}(\mathbf{v}_*^{n+1}),$$

where the last term corresponds to the convective terms and the symbol

$$\mathbf{v}_*^{n+1} = 2\mathbf{v}^n - \mathbf{v}^{n-1}$$

denotes the linearly extrapolated “predictor” of the velocity. In such case, the CGM must be replaced by other suitable algorithms like GMRES or BiCGStab. In any case, rate of convergence of the velocity solver is expected to drop and more sophisticated preconditioning techniques are needed. Consequently, the computation based of direct solution of the Uzawa system (3.10b) may become prohibitively expensive.

A possible way to circumvent this difficulty is to replace the matrix  $\mathbf{C}^{-1}$  in the formula (3.11) by some suitable approximation. A simple option is to write

$$(3.13) \quad \mathbf{C}^{-1} \approx \frac{2\Delta t}{3} \mathbf{M}_V^{-1} \equiv \mathbf{H},$$

which means replacement in (3.10b) of the exact Uzawa matrix  $\mathbf{\Sigma}$  by its (still symmetric and positive definite) approximation

$$(3.14) \quad \mathbf{S} = -\mathbf{B}\mathbf{H}\mathbf{B}^T.$$

The advantage in term of computational efficiency is obvious – the multiplication of any vector by the matrix  $\mathbf{S}$  requires now only the inversion of the mass matrix  $\mathbf{M}_V$  instead of a full matrix  $\mathbf{C}$ . However, in the nodal variant of the spectral element method, the matrix  $\mathbf{M}_V$  is diagonal, so its inversion is trivial. The numerical method based on such approximation of the Uzawa matrix is called the basic Yosida method.

It can be shown (see [6], [7] and the Appendix A) that the Yosida method can be interpreted as a discrete version of a quasi-compressibility approach. This method can be also viewed as the realization of the inexact block-LU decomposition of the original system (3.8). This point of view is particularly fruitful because it opens path to higher order variants of the Yosida method. The systematic exposition of this theory can be found in the original papers [7] and [8]. For the sake of self-sufficiency, the derivation of the high-order Yosida methods is outlined also in the Appendix A.

#### 4. Discussion of results

In this section, the obtained results are discussed. As it was already mentioned, these results have been obtained by using two kinds of the Stokes/Navier–Stokes in-house solvers: the ESEM solver, in which the continuity constrain is enforced exactly, and the YSEM solver which implements the Yosida method of an arbitrary order.

##### 4.1. The test flows

The test cases considered in this study are pulsatile Stokes and Navier–Stokes flows past the obstacle in the form of the square confined between parallel walls of the 2D channel. The height of this channel (the distance between the walls) is equal  $1\ lu$  (length unit). The square obstacle is rotated by 45 degrees with respect to the walls. The length of its diagonal is equal  $0.5\ lu$ , i.e., the blockage ratio is 50%. The length of the computational domain is equal  $2\ lu$ . The kinematic viscosity is set to  $0.01\ lu^2/tu$ , where  $tu$  is the time unit. If  $l = 1\ \text{cm}$  and

$tu = 1$  s, this value corresponds to the viscosity of water at the temperature of  $20^\circ$  C.

All variants of the SEM solvers use the same mesh containing 640 spectral elements. The order of the spectral elements has varied in this study from  $(N_V, N_P) = (5, 3)$  to  $(N_V, N_P) = (9, 7)$ , with mostly used reference setting  $(N_V, N_P) = (7, 5)$ . The open boundary conditions are applied at both inlet and outlet, as described in the previous section. Each case of the flow is accelerated from rest and – after a short transient – it is driven by a periodically modulated pressure difference. The period of this sinusoidal modulation is equal 0.2. In each case, the time duration of the computed flow is equal 2.

In Figure 2, the time history of the inlet section-averaged pressure  $P_{in}$  and the volumetric flow rate corresponding to the Stokes and Navier–Stokes flows are presented. Both flows were computed by the ESEM solver, with the spectral elements  $(N_V, N_P) = (7, 5)$  and the time step  $\Delta t = 0.0002$ . It can be seen that the time interval covered by the simulation is sufficiently long for the Navier–Stokes flow to achieve a time-periodic state, while the Stokes flow is still accelerating. In the periodic regime, the volumetric flow rate of the Navier–Stokes flow oscillates around the value of 5, meaning that the average Reynolds number of this flow (based on the average velocity and the vertical dimension of the obstacle) is approximately equal 250.

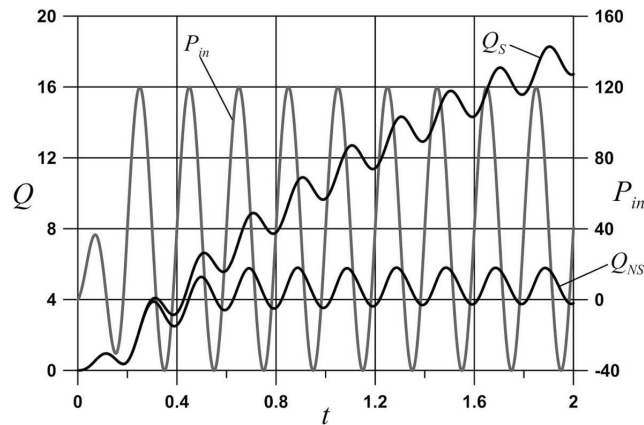


FIG. 2. Time variation of the section-averaged inlet pressure  $P_{in}$  and the volumetric flow rates of the Stokes ( $Q_S$ ) and the Navier–Stokes ( $Q_{NS}$ ) test flows.

The instantaneous Stokes flow pattern at the time  $t = 2$  is presented in Fig. 3. Analogous results for the Navier–Stokes flow are depicted in Fig. 4. One can see that the symmetry of the Navier–Stokes flow is maintained by the end of the simulation time. It is worth mentioning that the global volume balance in both

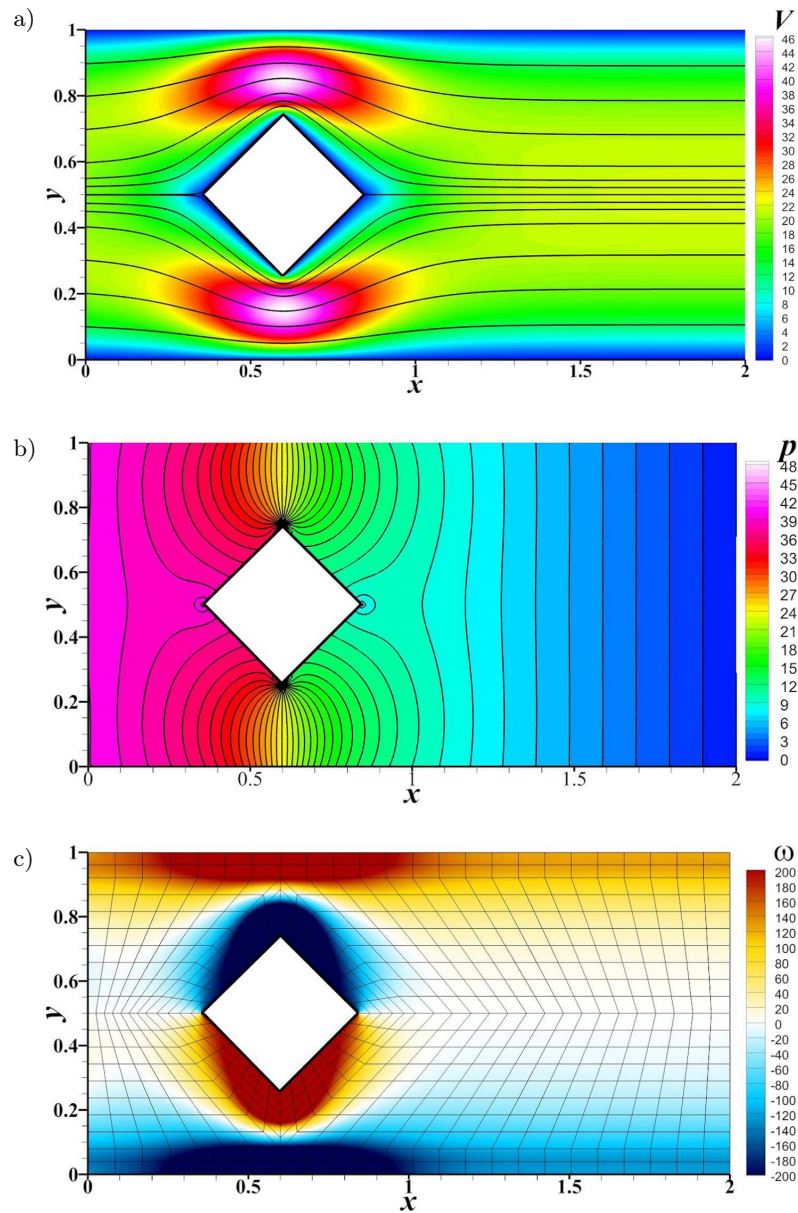


FIG. 3. Instantaneous velocity magnitude (with streamlines) (a), pressure (b) and vorticity (c) fields of the test Stokes flow computed at  $t = 2$ .

flows determined by the ESEM solver is nearly perfect – the difference between inlet and outlet volumetric flow rate is at the level of  $10^{-14}$ , i.e., close to machine accuracy.

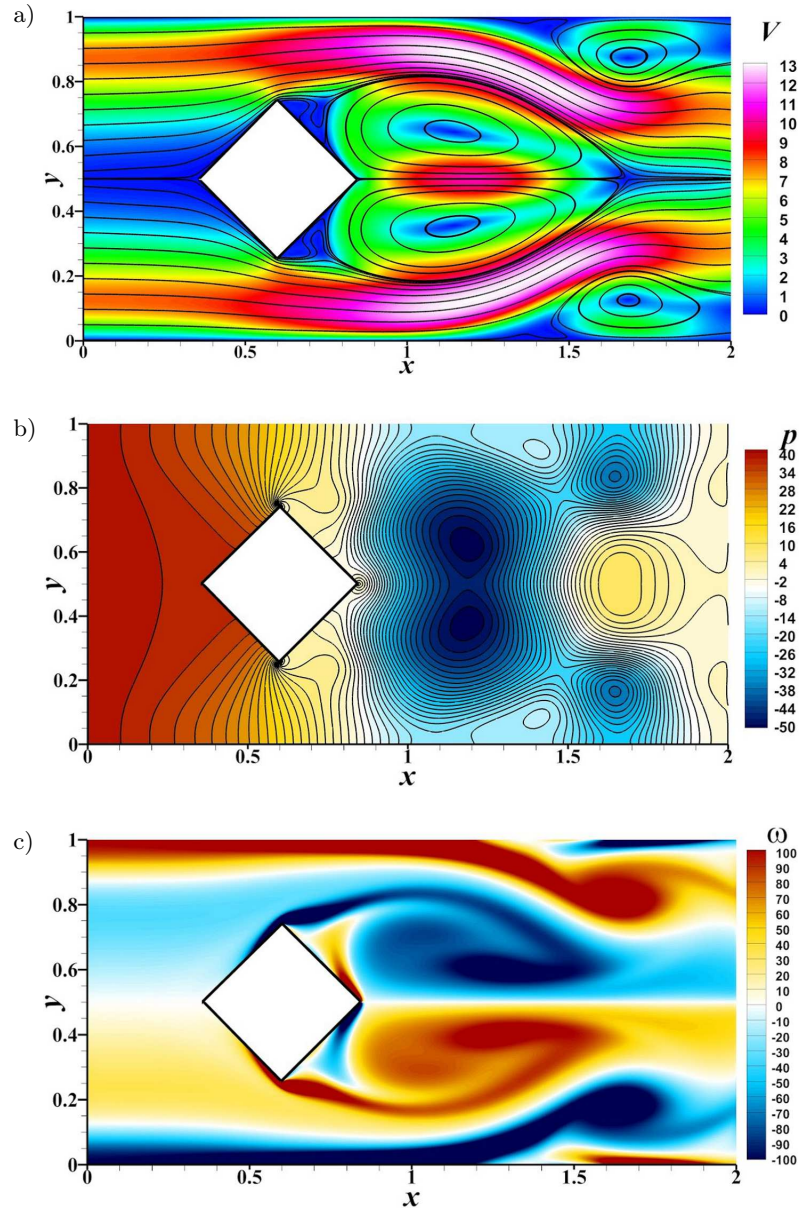


FIG. 4. Instantaneous velocity magnitude (with streamlines) (a), pressure (b) and vorticity (c) fields of the test Navier–Stokes flow computed at  $t = 2$ .

Since the obstacle has geometric singularities, i.e., sharp convex corners, one can expect concentration of large errors in flow quantities defined by spatial differentiation, including the divergence of the velocity field. This effect is clearly

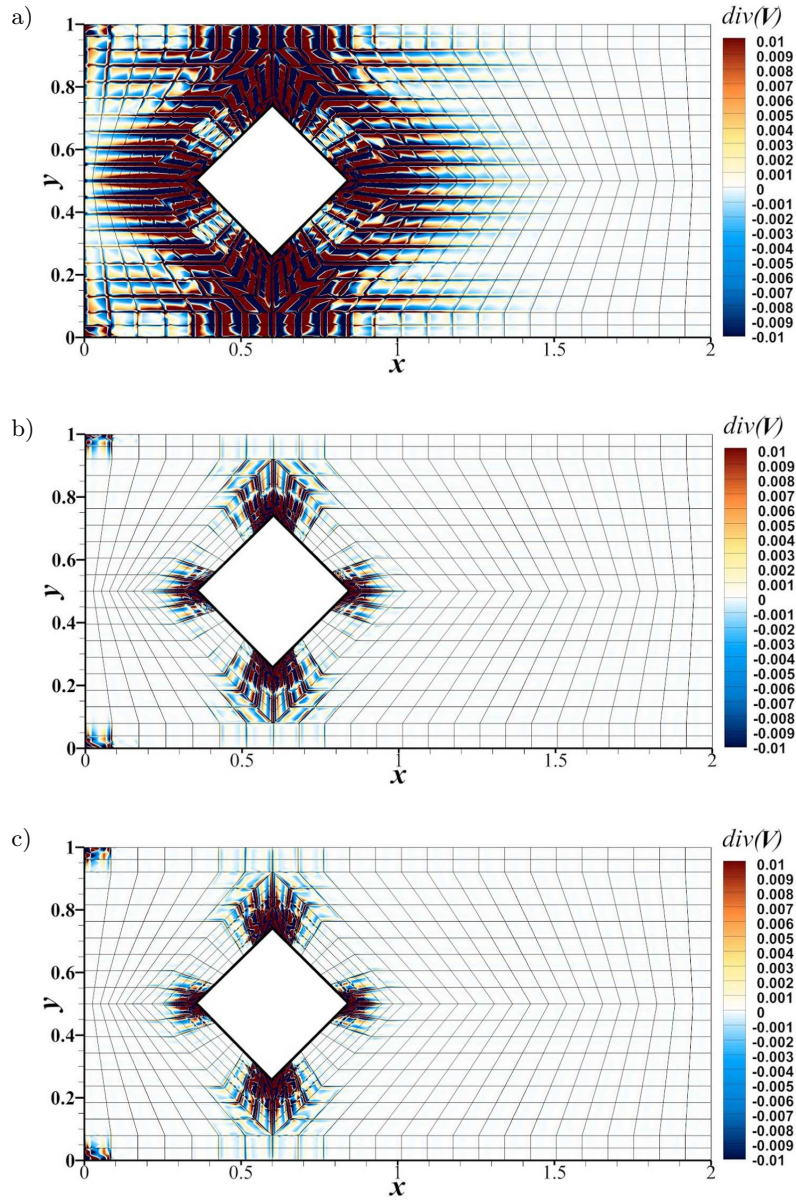


FIG. 5. Divergence of the Stokes velocity field at  $t = 2$  computed by means of the ESEM solver using different order of spectral elements and time step: (a)  $(N_V, N_P) = (5, 3)$ ,  $\Delta t = 0.0001$ ; (b)  $(N_V, N_P) = (7, 5)$ ,  $\Delta t = 0.0001$ ; (c)  $(N_V, N_P) = (7, 5)$ ,  $\Delta t = 0.01$ .

seen in the sequence of the divergence contour maps computed for the Stokes flow and presented in Fig. 5. One can notice regions of high divergence error near the corners of the obstacle. In is also observed that insufficient spatial resolution

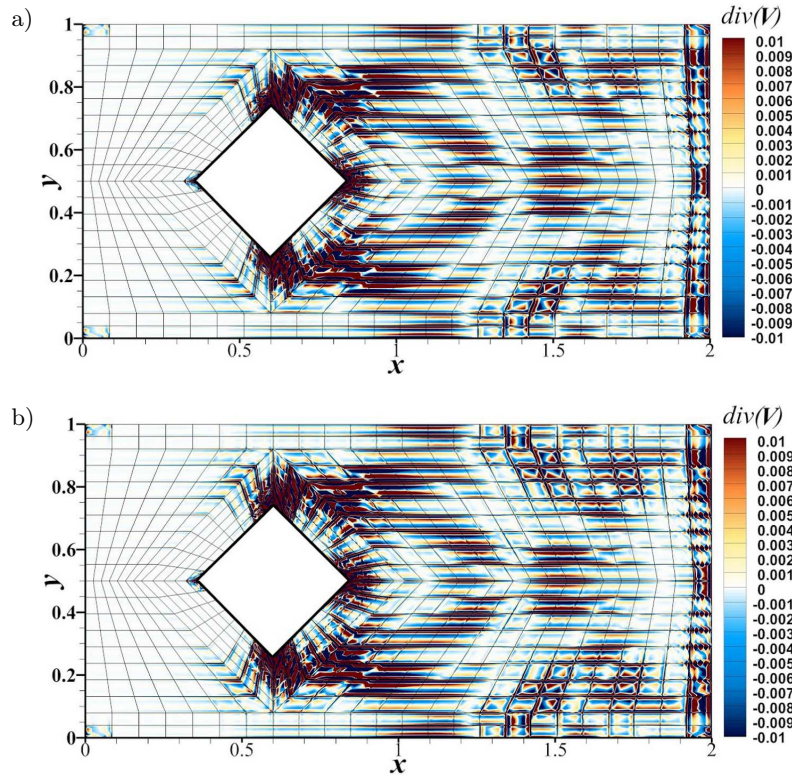


FIG. 6. Divergence of the Navier–Stokes velocity field at  $t = 2$  computed by means of the ESEM solver using the spectral elements with  $(N_V, N_P) = (7, 5)$  and different time step: (a)  $\Delta t = 0.0001$ ; (b)  $\Delta t = 0.0004$ .

(Fig. 5a) causes these regions to spread over larger portion of the flow domain. The situation is quite different when the time step is changed. As it is clear from Figs 5b and 5c, even substantial change of the time step does not influence much the size of the high-error concentration areas. Analogous results for the Navier–Stokes flow (due to stability limitations, time step variation is much smaller) are presented in Fig. 6. In this figure, one can notice essential differences between the divergence error distribution of Stokes and Navier–Stokes flows. First, in the latter there is no large divergence error region around the upstream corner. Secondly, the divergence error in the Stokes flow behind the obstacle is very low, while in the Navier–Stokes wake flow spindle-shaped regions with relatively large magnitude of the divergence error are clearly visible. Additionally, there is a concentration of the error along the layer of spectral elements adjacent to the outlet  $\Gamma_{out}$ . Note that such concentration is absent in the Stokes flow, even though the outflow boundary condition is the same.

**4.2. Spatial distribution of the divergence error in the Yosida methods**

In this section, we present the results concerning modifications in the spatial distribution of the velocity divergence error caused by switching from “exact” solvers (ESEM) to Yosida-based solvers (YSEM) with different values of the order parameter  $K$ , see Appendix A.

Application of the basic Yosida method (i.e., with  $K = 0$ ) to the Stokes flow brings results presented in Fig. 7, which shows the spatial distribution of the divergence error corresponding to different time steps. It is apparent that, besides corner effects already seen in ESEM simulations, new region of a high divergence error appears at the inlet to the flow domain. The characteristic wave-like spatial pattern of this error is confined to the first layer of the spectral elements adjacent to the inlet line. The magnitude of this error decreases rapidly with the time step reduction, as demonstrated in Figs 8a and 8b for the second-order Yosida method.

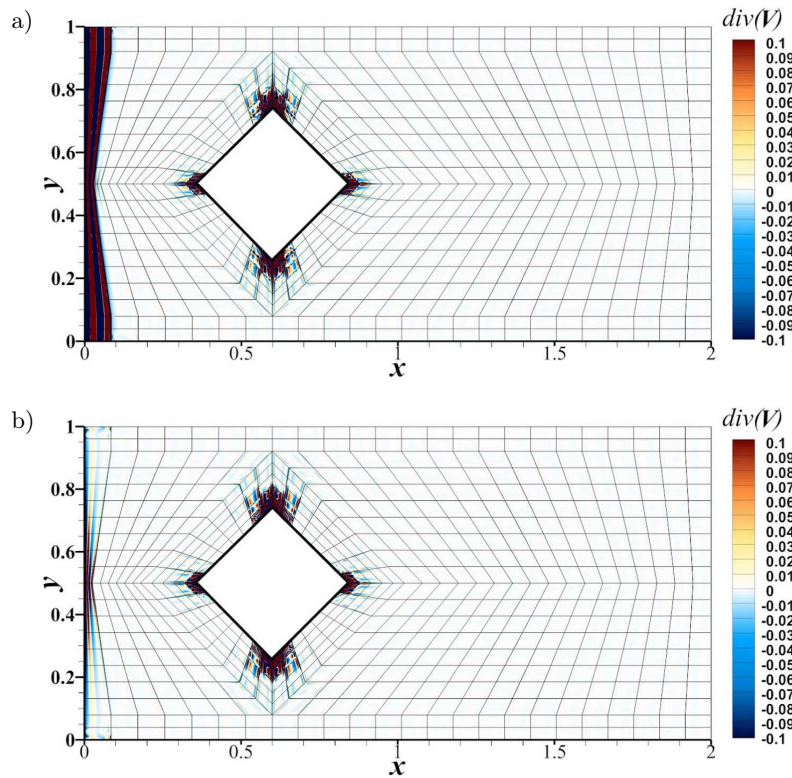


FIG. 7. Divergence of the Stokes velocity field at  $t = 2$  computed by the YSEM solver using basic Yosida method ( $K = 0$ ), the spectral elements  $(N_V, N_P) = (7, 5)$  and the time step: (a)  $\Delta t = 0.0008$ ; (b)  $\Delta t = 0.0001$ .

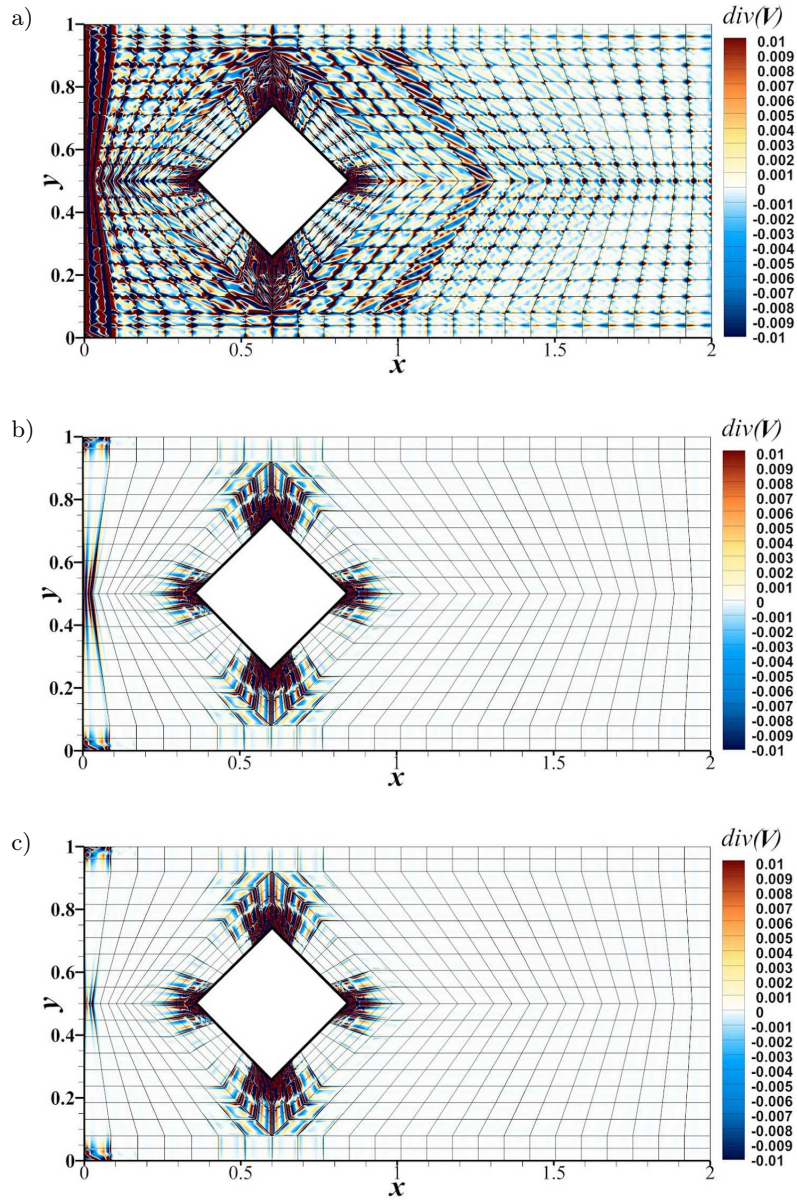


FIG. 8. Divergence of the Stokes velocity field at  $t = 2$  computed by the YSEM solver using spectral elements  $(N_V, N_P) = (7, 5)$  and: (a) second-order Yosida method ( $K = 1$ ) and  $\Delta t = 0.0008$ ; (b) second-order Yosida method ( $K = 1$ ) and  $\Delta t = 0.0002$ ; (c) third-order Yosida method ( $K = 2$ ) and  $\Delta t = 0.0002$ .

Rising the order of the Yosida method also leads to substantial reduction of the inlet divergence error. This effect is depicted in the Figs 8b and 8c,

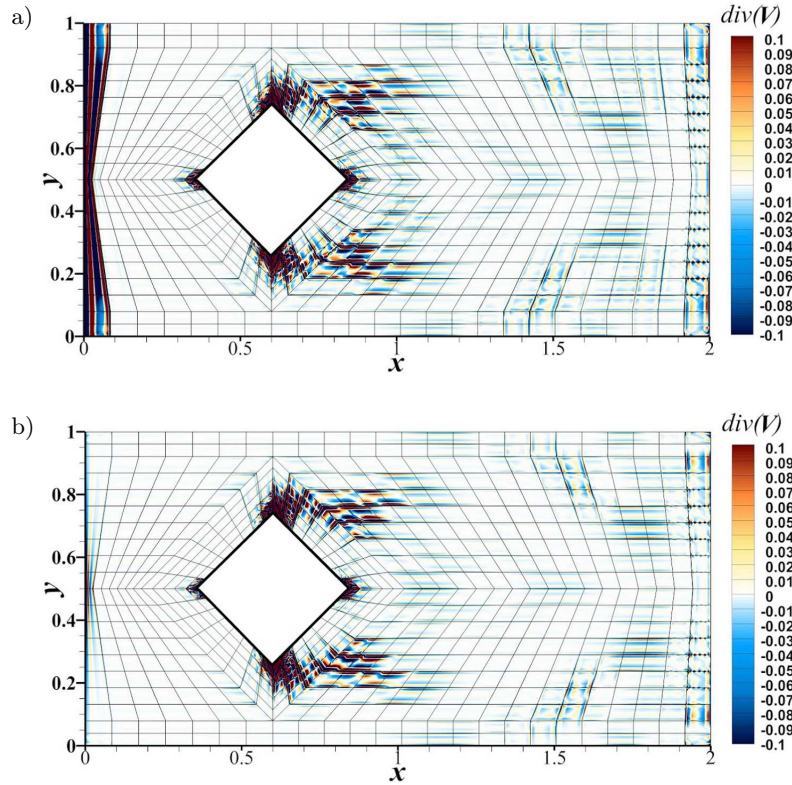


FIG. 9. Divergence of the Navier–Stokes velocity field at  $t = 2$  computed by means of the YSEM solver using the basic Yosida method ( $K = 0$ ), spectral elements  $(N_V, N_P) = (7, 5)$  and the time step: (a)  $\Delta t = 0.0004$ , (b)  $\Delta t = 0.0001$ .

which show the divergence of the Stokes flow computed by the second-order ( $K = 1$ ) and third-order ( $K = 2$ ) Yosida methods with the same time step  $\Delta t = 0.0002$ .

Similar results have been obtained for the Navier–Stokes flow. Figure 9 present the spatial distribution of the velocity divergence obtained with the basic Yosida method ( $K = 0$ ) for two different time steps. The inlet errors of the same sort as in the Stokes flow appear again, with the strong tendency to drop with decreasing time step. The same effect is observed for the higher-order Yosida methods, see Figs 10a and 10b. Again, high divergence error along the inlet line can be further reduced by switching to higher-order variant of the Yosida method. In fact, the spatial distribution of the velocity divergence error obtained from the third-order Yosida method with  $\Delta t = 0.0001$ , shown in the Fig. 10c, is essentially undistinguishable from the result obtained from the ESEM solver with the same order of spatial discretization.

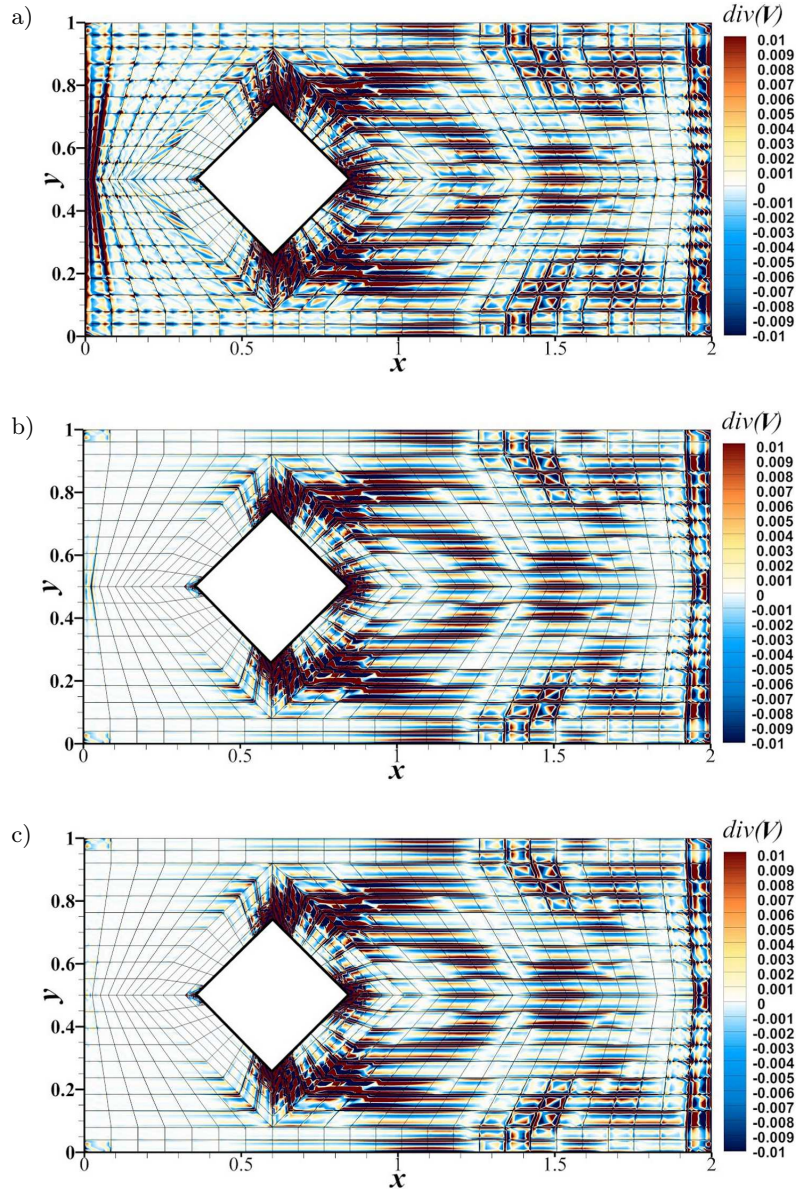


FIG. 10. Divergence of the Navier–Stokes velocity field at  $t = 2$  computed by the YSEM solver using spectral elements  $(N_V, N_P) = (7, 5)$  and: (a) second-order Yosida method ( $K = 1$ ) and  $\Delta t = 0.0004$ ; (b) second-order Yosida method ( $K = 1$ ) and  $\Delta t = 0.0001$ ; (c) third-order Yosida method ( $K = 2$ ) and  $\Delta t = 0.0001$ .

#### 4.3. Global flow rate error

By the global flow rate error (FRE) we mean the difference between the flow rates at the inlet and outlet of the computational domain. It has been already

mentioned that in the ESEM simulations this error is essentially at the machine accuracy level. Obviously, it is not the case for the Yosida schemes, since the continuity constrain is enforced only approximately. In the current study, we investigated the variations of the FRE related to the order of the spectral element approximation and to the time integration step. Eventually, we also assessed the effect of increasing the order of the Yosida method.

The time variation of the FRE for selected test cases of Stokes and Navier–Stokes flows are presented in Fig. 11. A common (and paradoxical) conclusion from all computed cases is that application of higher-order spectral approximation leads to larger flow error. In other words, spatially unresolved simulations performed better if the global volume balance is concerned. Another surprising effect is that the FRE computed for the Stokes flow oscillates in time with a fixed amplitude (except short initial transient) while the flow itself is continuously accelerating during the simulation time interval. This means that the relative accuracy of the volume conservation in the Stokes flow improves in time.

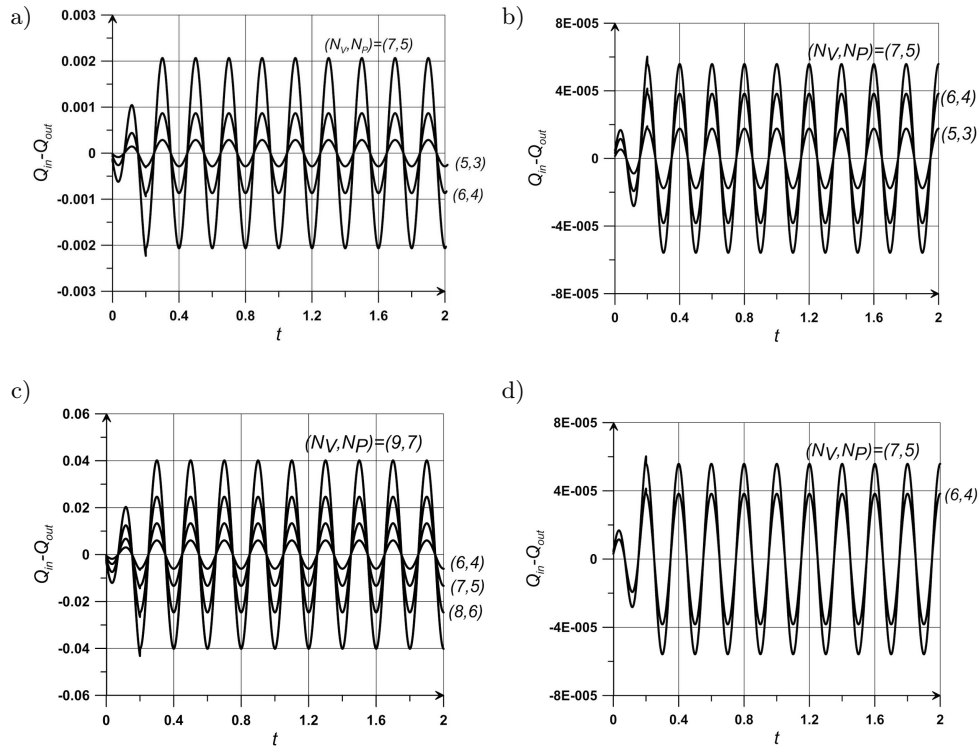


FIG. 11. The time variation of the flow rate error (FRE) computed with the use of different orders of spectral elements and the Yosida method (parameter  $K$ ): (a) Stokes flow,  $K = 0$ , (b) Stokes flow,  $K = 1$ , (c) Navier–Stokes flow,  $K = 0$ , (d) Navier–Stokes flow,  $K = 1$ . In all presented cases the time step is  $\Delta t = 0.0002$ .

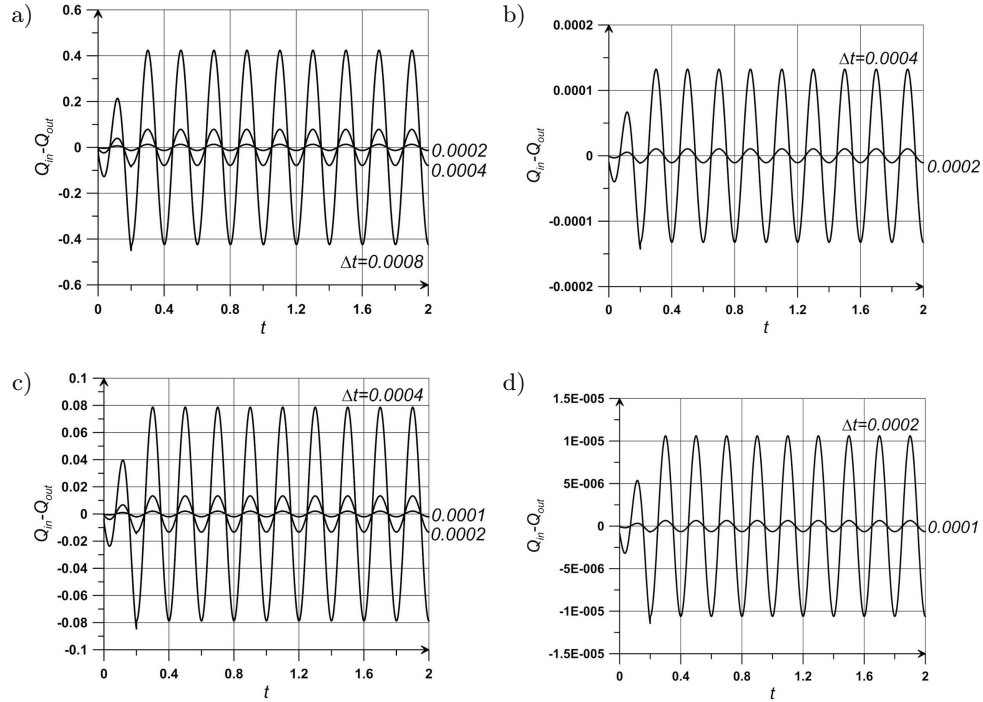


FIG. 12. The time variation of the flow rate error (FRE) obtained from YSEM solver for: (a) the Stokes flow,  $K = 0$ ; (b) the Stokes flow,  $K = 2$ ; (c) the Navier–Stokes flow,  $K = 0$ ; (d) the Navier–Stokes flow,  $K = 2$ . In all presented cases, the spectral elements  $(N_V, N_P) = (7, 5)$  have been used.

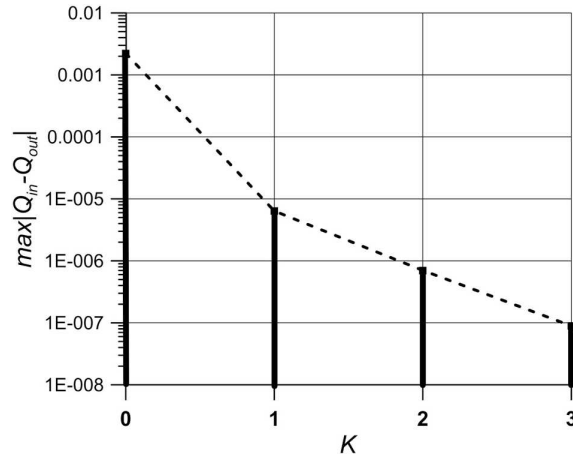


FIG. 13. The maximal flow rate error in the time period  $[0, 2]$  computed for the Navier–Stokes flow obtained from the YSEM solvers with different order parameter  $K$ . The spectral elements used are  $(N_V, N_P) = (7, 5)$  and the time step is  $\Delta t = 0.0001$ .

The reduction of the time step leads to rapid improvement of the global volume balance in the flow domain. It is clearly seen from the plots in Fig. 12 which show FRE variations in time computed for selected cases of Stokes and Navier–Stokes flows. One can also notice remarkable effect of increasing the order of the Yosida method. The dramatic reduction of the FRE in the YSEM simulations of the Navier–Stokes flow with increasing order  $K$  is illustrated in Fig. 13. Particularly large improvement in accuracy – more than by two orders of magnitude – is observed when switching from basic  $K = 0$  to  $K = 1$ .

## 5. Conclusion and outlook

In this study, the Yosida methods of different orders have been applied to the nonstationary two-dimensional Stokes and Navier–Stokes flows past the obstacle confined between parallel walls of the 2D channel in order to assess the local and global errors of the volume conservation. The main conclusions from this investigation can be summarized as follows:

1. Low-order Yosida method combined with the open boundary conditions at the inlet to the computational domain may generate oscillatory pattern of large divergence error along the inlet. The amplitude of these oscillations increases with the simulation time step.
2. The effective remedy to the above-mentioned effect is switching to higher-order Yosida schemes.
3. The amplitude of time oscillations of the flow rate error (FRE) rises with the order of spectral element approximation. This is effect is persistent in all test cases considered in this study.
4. Reduction of the time step as well as rising the order of the Yosida method are very effective ways of reduction of the flow rate error. In the test cases considered in this study, rising the Yosida method's order by the unity causes reduction of the FRE by roughly one order of magnitude. The improvement in accuracy is especially large while switching from the basic to second-order Yosida method.

In this study, we have concentrated only on the problem of volume conservation. There are, however, other issues which determine (and possibly limit) the practical use of the Yosida methods: stability and numerical cost. The experience of the current investigation is that the YSEM solvers are generally less stable than ESEM solvers. The stability limits become more restricted when the order of the Yosida method rises. This means that the time step must be

reduced which – together with the higher computational cost of each time step – may make the overall numerical effort prohibitive. The key problem is how to solve efficiently the linear system with the “pseudo-Uzawa” matrix  $\mathbf{S}$  (see Appendix A), which should be done  $K$  times in each time step of the  $K$ th-order Yosida method. Although multiplication of a vector by the matrix  $\mathbf{S}$  is much cheaper than by the exact Uzawa matrix  $\mathbf{\Sigma}$ , the former matrix is still very poorly conditioned, hence efficient preconditioning technique is mandatory. The preconditioner implemented in the YSEM solvers used in this research is based on the P5 preconditioner proposed originally by COUZY and DEVILLE [13] and used in the ESEM solvers for the linear system with the Uzawa matrix  $\mathbf{\Sigma}$ . The P5 preconditioner is quite complex and essentially works on two levels. The upper level corresponds to the main iterative procedure for the pressure system with the exact Uzawa matrix  $\mathbf{\Sigma}$ . At this level, a small (and usually fixed) number of the CGM iterations is applied to the matrix  $\mathbf{S}$  to boost the convergence rate of the pressure solver. Although in practice the convergence of these iterations is neither achieved nor needed, they are preconditioned by the low-level block-diagonal preconditioner combined with direct diagonalization and oblique projection (see [14] for details).

In a Yosida-based solver, the linear system with the matrix  $\mathbf{\Sigma}$  is never solved. Instead, one has to solve the linear system with the matrix  $\mathbf{S}$  at least once in each time step and, in contrast to the practice described above, the corresponding iterative process must be fully convergent. The P5 low-level preconditioning technique can be easily adopted for this purpose. This solution has been implemented in the YSEM Stokes and Navier–Stokes solvers used in this study.

In the test cases considered in this study, full convergence of the CGM applied to the system with  $\mathbf{S}$  matrix and P5-based preconditioner required typically around 100 iterations. In the ESEM solvers, the fixed number of 10–12 iterations of the low-level preconditioner allows the external iterative process (i.e., the pressure solver) to converge in a few iteration steps. Hence, the computational performance of the higher-order Yosida solvers seems to be worse than of the ESEM solvers. However, it should be mentioned that good performance of the ESEM pressure solver results not only from efficient preconditioning but also thanks to the smart initialization of the CGM iterations based on the Fisher’s projection method [15]. In the current version of YSEM solvers, latter technique has not yet been implemented. Hence, the outcome of the performance comparison may change when an improved version of the YSEM solvers appears.

We also believe that a real advantage of the higher-order Yosida methods will be demonstrated when the convective terms in the Navier–Stokes equations are treated in semi-implicit manner rather than by the OIFS method. In such case, the matrix  $\mathbf{C}$  is defined by (3.12) and it is neither symmetric nor positive definite. Consequently, multiplication of any vector by the exact Uzawa matrix

$\Sigma$  requires now the solution of the linear system with the matrix  $\mathbf{C}$  which is expected to be much more difficult and time consuming. Moreover, the matrix  $\Sigma$  is also not symmetric, hence the exact pressure system is much harder to solve and preconditioned effectively.

In the Yosida method, there are only two changes, none of them being a real nuisance:

1. the determination of the velocity field (initial and final) would require now solution of the linear system with the non-symmetric matrix  $\mathbf{C}$  (four or six times, dependently of the spatial dimension) and
2. evaluation of the product of the matrix  $\mathbf{C}$  by a few different vectors while calculating the right-hand side vectors for the linear system with the matrix  $\mathbf{S}$  in the pressure solving stage.

Since stability thresholds offered by the OIFS are rather limited, more stable treatment of convective nonlinearities based on the higher-order Yosida method will be developed to improve performance of the in-house spectral element solvers.

### Appendix A: The Yosida method ([7], [8])

In the Section 3, we have presented the three-step solution procedure (3.10) for the linear system (3.8). This procedure can be viewed as the application of the block-LU factorization

$$(A1) \quad \begin{bmatrix} \mathbf{C} & \mathbf{B}^T \\ \mathbf{B} & \mathbf{0} \end{bmatrix} = \begin{bmatrix} \mathbf{C} & \mathbf{0} \\ \mathbf{B} & \Sigma \end{bmatrix} \begin{bmatrix} \mathbf{I} & \mathbf{C}^{-1}\mathbf{B}^T \\ \mathbf{0} & \mathbf{I} \end{bmatrix} \equiv \mathbf{L}\mathbf{U},$$

where  $\Sigma = -\mathbf{B}\mathbf{C}^{-1}\mathbf{B}^T$ . In order to avoid inversion of the matrix  $\mathbf{C}$  in the solution step (3.10b), we consider an inexact LU-decomposition

$$(A2) \quad \begin{bmatrix} \mathbf{C} & \mathbf{B}^T \\ \mathbf{B} & \mathbf{0} \end{bmatrix} \approx \begin{bmatrix} \mathbf{C} & \mathbf{0} \\ \mathbf{B} & \mathbf{S} \end{bmatrix} \begin{bmatrix} \mathbf{I} & \mathbf{C}^{-1}\mathbf{B}^T \\ \mathbf{B} & \mathbf{Q} \end{bmatrix} \equiv \tilde{\mathbf{L}}\tilde{\mathbf{U}},$$

where  $\mathbf{S} = -\mathbf{B}\mathbf{H}\mathbf{B}^T$ ,  $\mathbf{H} = \frac{\Delta t}{\alpha_0}\mathbf{M}_V^{-1}$  and  $\alpha_0$  denotes the coefficient of the time discretization scheme ( $\alpha_0 = 3/2$  for the second-order BDF scheme). With the factorization (A2), the procedure (3.10) is replaced by

$$(A3) \quad \begin{cases} \mathbf{C}\tilde{\mathbf{v}} = \mathbf{f}_1, \\ \mathbf{S}\tilde{\mathbf{p}} = \mathbf{f}_2 - \mathbf{B}\tilde{\mathbf{v}}, \end{cases} \quad \begin{cases} \mathbf{Q}\mathbf{p} = \tilde{\mathbf{p}}, \\ \mathbf{C}\mathbf{v} = \mathbf{C}\tilde{\mathbf{v}} - \mathbf{B}^T\mathbf{p}, \end{cases}$$

where an additional linear system with the matrix  $\mathbf{Q}$  must be solved for the vector  $\mathbf{p}$  representing the “real” pressure field.

The multiplication of approximate factors  $\tilde{\mathbf{L}}$  and  $\tilde{\mathbf{U}}$  in (A2) yields

$$(A4) \quad \begin{bmatrix} \mathbf{C} & \mathbf{0} \\ \mathbf{B} & \mathbf{S} \end{bmatrix} \begin{bmatrix} \mathbf{I} & \mathbf{C}^{-1}\mathbf{B}^T \\ \mathbf{B} & \mathbf{Q} \end{bmatrix} = \begin{bmatrix} \mathbf{C} & \mathbf{B}^T \\ \mathbf{B} & \mathbf{B}\mathbf{C}^{-1}\mathbf{B}^T + \mathbf{S}\mathbf{Q} \end{bmatrix} = \begin{bmatrix} \mathbf{C} & \mathbf{B}^T \\ \mathbf{B} & -\mathbf{\Sigma} + \mathbf{S}\mathbf{Q} \end{bmatrix}.$$

Ideally, i.e., when  $\mathbf{\Sigma} = \mathbf{S}\mathbf{Q}$ , the (2, 2) block in the obtained matrix is equal zero and the factorization is exact. If not, then the factorized system is not equivalent to the original system (A1). More precisely, inexact factorization introduces the error in this part of the system which corresponds to the continuity equation. Therefore, the procedure can be viewed as the algebraic variant of the quasi-compressibility approach.

It is possible to construct such  $\mathbf{Q}$  that the (2, 2) block of the product matrix in (A4) vanishes rapidly with the time step, namely for any given  $K \geq 0$

$$(A5) \quad \mathbf{\Sigma} - \mathbf{S}\mathbf{Q} = O(\Delta t^{K+1}).$$

Since the matrix  $\mathbf{\Sigma}$  is  $O(\Delta t)$ , the parameter  $K$  is the actual order of approximation.

Following [8] we will outline the procedure leading to the Yosida methods of arbitrary order  $K$ . In the first step, we define the matrices

$$\mathbf{W}_k = \mathbf{B}(-\mathbf{H}\mathbf{R})^k \mathbf{H}\mathbf{B}^T, \quad k = 0, 1, 2, \dots,$$

where  $\mathbf{R} = \mathbf{C} - \frac{\alpha_0}{\Delta t} \mathbf{M}_V$  (here  $\mathbf{R} = \nu \mathbf{K}_V$ ). Note that the norms  $\|\mathbf{W}_k\| = O(\Delta t^{k+1})$ . Next, we construct the matrix  $\mathbf{D} = \mathbf{S}^{-1} \sum_{k>0} \mathbf{W}_k$ , which norm is  $\|\mathbf{D}\| = O(\Delta t)$ . Hence, for sufficiently small  $\Delta t$  the spectral radius of the matrix  $\mathbf{D}$  is less than 1. The same is true about the product  $\mathbf{H}\mathbf{R}$  which is also  $O(\Delta t)$ . Eventually, the matrix  $\mathbf{\Sigma}$  can be expressed as follows

$$(A6) \quad \begin{aligned} \mathbf{\Sigma} &= -\mathbf{B} \left( \frac{\alpha_0}{\Delta t} \mathbf{M} + \mathbf{R} \right)^{-1} \mathbf{B}^T \\ &= -\mathbf{B} [\mathbf{H}^{-1} + \mathbf{R}]^{-1} \mathbf{B}^T = -\mathbf{B} [\mathbf{H}^{-1} (\mathbf{I} + \mathbf{H}\mathbf{R})]^{-1} \mathbf{B}^T \\ &= -\mathbf{B} (\mathbf{I} + \mathbf{H}\mathbf{R})^{-1} \mathbf{H}\mathbf{B}^T = -\sum_{k \geq 0} [\mathbf{B}(-\mathbf{H}\mathbf{R})^k \mathbf{H}\mathbf{B}^T] = \mathbf{S} - \sum_{k > 0} \mathbf{W}_k \end{aligned}$$

and its inverse can be written as

$$(A7) \quad \begin{aligned} \mathbf{\Sigma}^{-1} &= \left( \mathbf{S} - \sum_{k > 0} \mathbf{W}_k \right)^{-1} = \left( \mathbf{I} - \mathbf{S}^{-1} \sum_{k > 0} \mathbf{W}_k \right)^{-1} \mathbf{S}^{-1} \\ &= (\mathbf{I} - \mathbf{D})^{-1} \mathbf{S}^{-1} = \left[ \sum_{k \geq 0} \mathbf{D}^k \right] \mathbf{S}^{-1}. \end{aligned}$$

Hence,  $\Sigma^{-1}\mathbf{S} = \sum_{k \geq 0} \mathbf{D}^k$  and the ideal matrix  $\mathbf{Q}_{id} = \mathbf{S}^{-1}\Sigma = (\Sigma^{-1}\mathbf{S})^{-1}$ . Using (A7),  $\mathbf{Q}_{id}^{-1}$  can be written as

$$(A8) \quad \mathbf{Q}_{id}^{-1} = \Sigma^{-1}\mathbf{S} = \sum_{k \geq 0} \mathbf{D}^k = \mathbf{I} + \sum_{k > 0} \mathbf{D}^k.$$

Apparently, the next step is simply to approximate  $\mathbf{Q}_{id}^{-1}$  by truncating the series in (A8). However, it would not work since the matrix  $\mathbf{D}$  itself is defined by the infinite matrix summation. An appropriate trick is to construct a series of matrices  $\hat{\mathbf{D}}_k$ ,  $k = 1, 2, 3, \dots$ , which are defined by finite formulae and such that

$$(A9) \quad \sum_{k > 0} \mathbf{D}^k = \sum_{k > 0} \hat{\mathbf{D}}_k.$$

It has been shown in [8] that three first members of this series are

$$(A10) \quad \begin{aligned} \hat{\mathbf{D}}_1 &= \mathbf{S}^{-1}\mathbf{W}_1, & \hat{\mathbf{D}}_2 &= \mathbf{S}^{-1}\mathbf{W}_2 + (\mathbf{S}^{-1}\mathbf{W}_1)^2, \\ \hat{\mathbf{D}}_3 &= \mathbf{S}^{-1}\mathbf{W}_3 + \mathbf{S}^{-1}\mathbf{W}_1\mathbf{S}^{-1}\mathbf{W}_2 + \mathbf{S}^{-1}\mathbf{W}_2\mathbf{S}^{-1}\mathbf{W}_1 + (\mathbf{S}^{-1}\mathbf{W}_1)^3. \end{aligned}$$

The corresponding increasing-order approximation formulae for the inverse  $\mathbf{Q}^{-1}$  are

$$(A11) \quad \begin{aligned} \mathbf{Q}_0^{-1} &= \mathbf{I}, \\ \mathbf{Q}_1^{-1} &= \mathbf{I} + \mathbf{S}^{-1}\mathbf{W}_1, \\ \mathbf{Q}_2^{-1} &= \mathbf{I} + \mathbf{S}^{-1}(\mathbf{W}_1 + \mathbf{W}_2) + (\mathbf{S}^{-1}\mathbf{W}_1)^2, \\ \mathbf{Q}_3^{-1} &= \mathbf{I} + \mathbf{S}^{-1}(\mathbf{W}_1 + \mathbf{W}_2) + (\mathbf{S}^{-1}\mathbf{W}_1)^2 + \mathbf{S}^{-1}\mathbf{W}_1\mathbf{S}^{-1}\mathbf{W}_2 \\ &\quad + \mathbf{S}^{-1}\mathbf{W}_2\mathbf{S}^{-1}\mathbf{W}_1 + (\mathbf{S}^{-1}\mathbf{W}_1)^3 + \mathbf{S}^{-1}\mathbf{W}_3. \end{aligned}$$

Note that  $\mathbf{Q}_{id}^{-1} = \mathbf{Q}_K^{-1} + O(\Delta t^{K+1})$  hence, using  $\mathbf{Q}_K^{-1}$  corresponds to the method of the (formal) order  $K + 1$ . The case with  $K = 0$  ( $\mathbf{Q}^{-1} \approx \mathbf{Q}_0^{-1} = \mathbf{I}$ ) is the basic first-order Yosida method.

The formulae (A11) can be used in the solution procedure (A3), i.e., the pressure vector  $\mathbf{p}$  is obtained from the formula  $\mathbf{p} = \mathbf{Q}_K^{-1}\tilde{\mathbf{p}}$ . The complete procedure of the  $K$ -step Yosida method can be summarized as follows (see [9]):

**Step 1:**

$$\begin{cases} \mathbf{C}\tilde{\mathbf{v}} = \mathbf{f}_1 \Rightarrow \tilde{\mathbf{v}}, \\ \mathbf{S}\mathbf{z}_0 = \mathbf{f}_2 - \mathbf{B}\tilde{\mathbf{v}} \Rightarrow \mathbf{z}_0. \end{cases}$$

**Step 2:** For  $k = 1, \dots, K$ :

$$\mathbf{S}\mathbf{z}_k = \sum_{j=0}^{k-1} \mathbf{W}_{k-j}\mathbf{z}_j \Rightarrow \mathbf{z}_j.$$

**Step 3:**

$$\begin{cases} \mathbf{p} = \mathbf{Q}_K^{-1} \tilde{\mathbf{p}} = \sum_{k=0}^K \mathbf{z}_k, \\ \mathbf{C}\mathbf{v} = \mathbf{f}_1 - \mathbf{B}^T \mathbf{p} \Rightarrow \mathbf{v}. \end{cases}$$

### Appendix B: Operator-Integration-Factor-Splitting method ([10], [11])

Consider the evolutionary equation in the operator form

$$(B1) \quad \frac{d}{dt} \mathbf{v} = L\mathbf{v} + N(\mathbf{v}),$$

where  $L\mathbf{v}$  and  $N(\mathbf{v})$  are linear and nonlinear terms, respectively. Consider the time-dependent operator  $F(t_*, t)$  (parametrized by  $t_*$ ) such that

$$(B2) \quad \frac{d}{dt} [F(t_*, t)\mathbf{v}(t)] = F(t_*, t)L\mathbf{v}(t).$$

Assume also that  $F(t_*, t_*) = id$ , i.e., this operator reduces to identity when  $t = t_*$ . It follows from the Eq. (B1) and the postulated property (B2) that

$$(B3) \quad \left[ \frac{d}{dt} F(t_*, t) \right] \mathbf{v}(t) + F(t_*, t)N[\mathbf{v}(t)] = 0.$$

Consider the following initial value problem (again, parametrized with  $t_*$ )

$$(B4) \quad \begin{cases} \frac{d}{d\tau} \mathbf{u}(t_*, \tau) = N[\mathbf{u}(t_*, \tau)], \\ \mathbf{u}(t_*, \tau = t) = \mathbf{v}(t). \end{cases}$$

Then, from (B3) and (B4), one obtains

$$(B5) \quad \begin{aligned} \frac{d}{d\tau} [F(t_*, \tau)\mathbf{u}(t_*, \tau)] &= \left[ \frac{d}{d\tau} F(t_*, \tau) \right] \mathbf{u}(t_*, \tau) + F(t_*, \tau) \frac{d}{d\tau} \mathbf{u}(t_*, \tau) \\ &= -F(t_*, \tau)N[\mathbf{u}(t_*, \tau)] + F(t_*, \tau)N[\mathbf{u}(t_*, \tau)] = 0. \end{aligned}$$

Hence  $F(t_*, \tau)\mathbf{u}(t_*, \tau) = \text{const}$  and

$$(B6) \quad F(t_*, t)\mathbf{u}(t_*, t) = F(t_*, t_*)\mathbf{u}(t_*, t_*) = \mathbf{u}(t_*, t_*).$$

The formula (B6) has the following meaning: in order to calculate the action of the operator  $F(t_*, t)$  on the function  $\mathbf{v}(t) = \mathbf{u}(t_*, t)$  one needs to determine the solution to the initial value problem (B4) at the time  $\tau = t_*$ .

In order to construct a time integration scheme for the equation (B1) one can apply the  $M$ th-order backward differentiation formula (BDF) to the equation (B2) with  $t_* = t_{n+1}$ . This formula can be written as

$$(B7) \quad \frac{1}{\Delta t} [\alpha_0 F(t_{n+1}; t_{n+1}) \mathbf{v}(t_{n+1}) - \sum_{k=1}^M \alpha_k F(t_{n+1}; t_{n+1-k}) \mathbf{v}(t_{n+1-k})] = L \mathbf{v}(t_{n+1}),$$

where  $\alpha_0, \alpha_1, \dots, \alpha_N$  are the known coefficients. In order to avoid explicit reference to the operator  $F(t_*; t_k)$ ,  $k = n + 1 - M, n + 2 - M, \dots, n$ , the following initial value problems must be solved

$$(B8) \quad \begin{cases} \frac{d}{dt} \mathbf{u}^k(t) = N[\mathbf{u}^k(t)], & t \in [t_{n+1-k}, t_{n+1}] \\ \mathbf{u}^k(t = t_{n+1-k}) = \mathbf{v}(t_{n+1-k}) \end{cases} \quad k = 1, \dots, M.$$

Using (B6) one obtains the values  $\mathbf{u}_{n+1}^k \equiv \mathbf{u}^k(t_{n+1}) = F(t_{n+1}; t_{n+1-k}) \mathbf{v}(t_{n+1-k})$ ,  $k = 1, \dots, M$ . Using also the identity  $F(t_{n+1}; t_{n+1}) = \text{id}$ , the formula (B7) can be re-written as

$$(B9) \quad \frac{\alpha_0}{\Delta t} \mathbf{v}_{n+1} - L \mathbf{v}_{n+1} = \frac{1}{\Delta t} \sum_{k=1}^M \alpha_k \mathbf{u}_{n+1}^k.$$

In the CFD context, the solution of the initial value problems (B8) and (B9) involves numerical integration of the convective terms, typically by means of the fourth-order explicit Runge–Kutta method which combines reasonable numerical cost with good stability properties in convective-dominated problems. Low-storage variants of this method may be used for large problems to reduce the memory requirements.

### Acknowledgements

The author acknowledges support from a research project funded by the Polish National Science Centre (contract number UMO-2011/01/B/ST8/07267).

### References

1. J.-L. GUERMOND, P. MINEV, J. SHEN, *An overview of projection methods for incompressible flows*, Computer Methods in Applied Mechanics and Engineering, **195**, 6011–6045, 2006.
2. J.-L. GUERMOND, *Overview of fractional step techniques for the incompressible Navier–Stokes equations*, CEMRACS’12 talk. CIRM, Marseille, July 16–20, 2012.

3. H. JOHNSTON, J.-G. LIU, *Accurate, stable and efficient Navier–Stokes solvers based on explicit treatment of the pressure term*, Journal of Computational Physics, **199**, 221–259, 2004.
4. J.-G. LIU, L. LIU, R.L. PEGO, *Stable and accurate pressure approximation for unsteady incompressible viscous flow*, Journal of Computational Physics, **229**, 3428–3453, 2010.
5. J.B. PEROT, *An analysis of the fractional step method*, Journal of Computational Physics, **108**, 51–58, 1993.
6. A. QUARTERONI, F. SALERI, A. VENEZIANI, *Analysis of the Yosida method for the incompressible Navier–Stokes equations*, J. Math. Pures Appl., **78**, 9, 473–503, 1999.
7. A. QUARTERONI, F. SALERI, A. VENEZIANI, *Factorization methods for the numerical approximation of Navier–Stokes equations*, Computer Methods in Applied Mechanics and Engineering, **188**, 505–526, 2000.
8. P. GERVASIO, F. SALERI, A. VENEZIANI, *Algebraic fractional-step schemes with spectral methods for the incompressible Navier–Stokes equations*, Journal of Computational Physics, **214**, 347–365, 2006.
9. A. VENEZIANI, U. VILLA, *ALADINS: An ALgebraic splitting time ADaptive solver for the Incompressible Navier–Stokes equations*, Journal of Computational Physics, **238**, 359–375, 2013.
10. Y. MADAY, A.T. PATERA, E.M. RONQUIST, *An operator-integration-factor splitting method for time-dependent problems: application to incompressible fluid flow*, Journal of Scientific Computing, **5**, 263–292, 1990.
11. M.O. DEVILLE, P.F. FISHER, E.H. MUND, *High-Order Methods for Incompressible Fluid Flow*, Cambridge University Press, 2002.
12. G.E. KARNIADAKIS, S. SHERWIN, *Spectral/hp Element Methods for CFD*, 2nd ed., Oxford University Press, 2005.
13. W. COUZY, M.O. DEVILLE, *Spectral-element for the Uzawa pressure operator applied to incompressible flows*, J. Scientific Computing, **9**, 2, 107–122, 1994.
14. J. SZUMBARSKI, P. OLSZEWSKI, K. WAWRUCH, Z. MAŁOTA, *Computations of an unsteady viscous flow in a three dimensional system of ducts. Part 2: Implementation of spectral element method and sample results*, Journal of Theoretical and Applied Mechanics, **42**, 4, 869–903, 2004.
15. P.F. FISHER, *Projection techniques for iterative solution of  $\mathbf{Ax} = \mathbf{b}$  with successive right-hand sides*, Computer Methods in Applied Mechanics and Engineering, **163**, 193–204, 1998.

Received August 13, 2015; revised version March 20, 2016.

---